Journal of Power Sources 399 (2018) 264–273

Contents lists available at ScienceDirect

Journal of Power Sources

journal homepage: www.elsevier.com/locate/jpowsour

Combined experimental and modeling approaches of the thermal runaway of fresh and aged lithium-ion batteries

Sara Abada[a,b], Martin Petit[a], Amandine Lecocq[b], Guy Marlair[b,*], Valérie Sauvant-Moynot[a], François Huet[c]

[a] IFP Energies Nouvelles, Rond-Point de l'échangeur de Solaize, BP 3, F-69360, Solaize, France
[b] INERIS, Parc Technologique Alata, BP 2, F-60550, Verneuil-en-Halatte, France
[c] Sorbonne Université, CNRS, Laboratoire Interfaces et Systèmes Electrochimiques, LISE, F-75005, Paris, France

HIGHLIGHTS

- Development of an original 3D thermal runaway model including calendar ageing.
- Model includes 3D thermal, 3D chemical reaction, and 0D calendar ageing sub-models.
- Calibration of the model for cylindrical 26650 LFP/C cells using a BTC.
- Validation of the model for fresh as well as 10% and 30% aged cells in oven tests.
- Fresh and aged cells are compared in terms of critical temperatures under overheating.

GRAPHICAL ABSTRACT

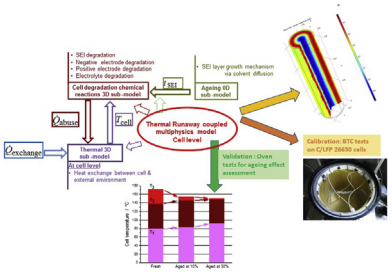

ARTICLE INFO

Keywords:
Li-ion battery modeling
Safety issues
Thermal runaway
Multiphysics modeling
Battery ageing
Electrochemical storage

ABSTRACT

Li-ion secondary rechargeable batteries are becoming the preferred solution to store energy on board of new generation electric and hybrid vehicles or manage renewable energy in stationary applications. However, Li-ion batteries (LIBs) are still suffering limited lifetime, high cost and significant safety issues increasing their time to mass market. Thermal runaway is still nowadays considered as a major hazard of LIBs. This multiscale and multistep phenomenon originating at the microscale level potentially leads to uncontrolled fire and explosion of the battery. This work is focused on the development and validation of a 3D physical model of the LIB electro-thermal behavior nearby thermal runaway conditions. A combined modeling and experimental investigation provides a better understanding of the mechanisms leading to thermal runaway of LIBs, and of the ageing influence on this process. One major outcome of this work is also the proven fact that calendar ageing leads to a delayed onset of the cell self-heating temperature with a thermal runaway starting at a lower temperature. This is supported by computer simulations showing that the thickening of the solid electrolyte interface (SEI) hinders the diffusion of Li ions, which delays the degradation of the negative electrode and the occurrence of thermal runaway.

* Corresponding author.
E-mail addresses: saraabada86@gmail.com (S. Abada), guy.marlair@ineris.fr (G. Marlair).

https://doi.org/10.1016/j.jpowsour.2018.07.094
Received 19 April 2018; Received in revised form 26 June 2018; Accepted 24 July 2018
0378-7753/

1. Introduction

Lithium-ion batteries (LIB) are currently considered as the best available solution to store energy on board of new generation of electrical, plug-in, or hybrid electrical vehicles, or to develop stationary applications with alternative green energy sources (solar, wind, photovoltaic). However, their ageing, high cost, and safety aspects still represent critical issues for these storage systems.

To assess and mitigate these drawbacks, major research efforts have been carried out in the recent past. Thermal runaway has been identified as a major concern with LIBs on the full value chain, potentially leading to uncontrolled fires and explosions causing the failure of the entire battery pack [1]. Catastrophic hazardous events reported to originate from LIBs, albeit not so frequent, such as violent venting, smoke, fire, explosion [2] still act as a clear restraint to LIB market development for high power/high energy applications, and still even in rare cases for consumer market appliances [3,4].

The thermal runaway of LIBs has been described as a multistep process implying a series of exothermic reactions related to the decomposition of different components of the cell (electrodes, electrolyte, and binder), together with their interactions occurring above a critical temperature, which led to an increased temperature inside the cell [5].

The most consensual analysis of the thermal runaway of a LIB considers that the phenomenon proceeds in four main stages occurring successively according to the onset of exothermic decomposition reactions as follows:

1. The first degradation reaction leading to the initial subsequent increase in cell temperature is usually reported to concern the solid electrolyte interface (SEI) that forms a passivation film on the surface of the carbon negative electrode. The onset of this reaction is ranging between 90 °C and 120 °C depending on the chemistry of the cell [6].
2. When the SEI starts to decompose, the electrolyte reacts violently with the active material of the negative electrode, which accelerates the cell temperature rise [7].
3. At temperatures above 120 °C [8], the positive electrode materials start to decompose, leading to evolution of oxygen that can react with the electrolyte and generate additional heat. According to thermal stability studies of commercial LIBs, the onset temperatures of the exothermic reactions at positive electrode materials rank in the following order:

$LiNiO_2$ (~180 °C) < $LiCoO_2$ (~200 °C) < $LiMn_2O_4$ (~220 °C) < $LiFePO_4$ (> 240 °C).

$LiFePO_4$ is then considered as the most thermally stable material of positive electrodes [7].

4. The electrolyte, most commonly a lithium salt dissolved in a mixture of organic carbonates, can decompose exothermically at elevated temperatures (> 200 °C) depending on its composition (salt, solvents, additives) [9].

At the cell level, the thermal runaway features globally depend on the chemistry of the cell components, as well as the shape and design of the cell [10]. They also depend on the state of charge (SOC) of the cell. Cells of higher SOC have revealed a lower thermal stability in dedicated studies, meaning a lower onset temperature of the thermal runaway reactions [5] and a higher self-sustained rate of increase of the cell temperature [11]. Some recent studies have investigated the effect of ageing on the thermal stability of cells by performing thermal stability tests under abuse conditions (overcharge, overheating …) to determine correlations between battery ageing and safety [12–15]. For example, the influence of cyclic ageing on the thermal behavior of Li-ion cells with $Li_xNi_{1/3}Mn_{1/3}Co_{1/3}O_2/Li_yMn_2O_4$-blend electrode positive materials was studied by Fleischhammer et al. [12]. They showed that cells aged by high-rate cycling had about the same safety behavior as fresh cells. In contrast, a significant increase of self-heating was observed for cells showing plating of metallic lithium on the negative electrode due to low temperature charging. On the other hand, Röder et al. [13] studied the influence of calendar ageing (at full SOC and 60 °C) on the thermal stability of a commercial Li-ion cell containing a mixture of $LiMn_2O_4$ and $Li(Ni_{1/3}Mn_{1/3}Co_{1/3})O_2$ as positive electrode material and graphite as negative electrode. They showed that the self-heating onset temperature of the aged cells was much lower than that of the fresh cells. These experimental studies show that the ageing history of aged cells plays a strong role on their safety so that an open issue is the way battery ageing affects its sensitivity to thermal runaway, in particular for the graphite-$LiFePO_4$ (LFP/C) technology claimed to be safer than the others.

So far, battery safety studies have mainly consisted in experimental approaches based on safety and abuse tolerance tests as well as post-mortem battery analyses [16]. However, these approaches show significant shortcomings due to the complexity of the phenomena involved in battery operation. Moreover, the safety and abuse tolerance tests are destructive so that the cost in battery test samples becomes an issue. Modeling and simulation are then used to predict battery performance and safety and help the design of new batteries, especially as experimental databases are now available for model calibration and validation, at least at cell level.

The number of investigations on LIB safety has increased in the last decade, including safety studies implementing modeling approaches [17–19]. However, battery modeling in abuse conditions was exclusively aimed for some time at modeling single events leading to battery failures as short circuit, mechanical abuse, overcharge or fire propagation. Combined modeling of electrical, chemical, and thermal behaviors of LIBs in abuse operating conditions emerged only after 2012. NREL (National Refreshable Energy Laboratory), Battery design LLC, and Sandia National Laboratories works constitute a large step forward in battery modeling and simulation in abuse conditions at different scales (cell/module/pack). However, all models of thermal runaway in abuse conditions available at the cell level are presently based on the chemical degradation reactions considered in Kim et al.'s model [6], none of them taking into account the influence of cell ageing. In this context, the objective of the present work is the development and validation of accurate physical models of the thermal behavior of fresh and aged LIBs in conditions leading to thermal runaway, for further practical applications to sizing and design support of safer batteries. A 3D thermal runaway model including ageing phenomena was developed and calibrated for cylindrical 26650 LFP/C cells (A123 Systems) using a battery test calorimeter (BTC) before validation with oven tests. The thermal safety of such LFP/C cells (fresh and aged at two different residual capacity) was then experimentally determined for comparison with expectations from the model to find out the influence of calendar ageing on battery safety.

2. Materials and methods

In order to build a multi-scale predictive model of thermal runaway adapted to fresh and aged LIBs, two complementary studies were carried out in parallel, a modeling work to develop several sub-models and achieve a coupled multi-physics and multidimensional model, and an experimental work to initially calibrate the sub-models and validate the model. As indicated above, A123 (2.3 Ah) cylindrical LFP/C cells were used. Their characteristics are presented in Table 1. All the tests were carried out with fully charged cells (100% SOC), which is known to be the worst-case scenario [5].

2.1. Modeling approach

As mentioned above, thermal runaway models available at the cell scale are all based on the chemical degradation reactions introduced in

Table 1
Characteristics of the cell under investigation (EC: Ethylene Carbonate, PC: Propylene Carbonate, EMC: Ethyl-Methyl Carbonate, NMP: N-Methyl Pyrrolidone, PP: PolyPropylene).

Cell technology	A123
Chemistry	LFP/C
Packaging	Cylindrical
Nominal capacity	2.3 Ah
Nominal voltage	3.2 V
Dimensions (D* h)	26 mm* 65 mm
Weight	77 g
Electrolyte	LiPF6 in EC-PC-EMC-NMP
Separator	PP

Kim et al.'s model [6] devoted to lithium-cobalt-oxide/carbon (LCO/C) technology. Reaction parameters were determined from accelerated rate calorimetry and differential scanning calorimetry tests, mainly performed by Hatchard and coworkers [20,21]. No effort has been made to validate Kim et al.'s model for the LFP/C technology and, to our knowledge, no degradation reaction parameters for this technology are available in the literature. Moreover, battery ageing phenomena have never been taken into account in thermal abuse models and their influence on thermal runaway has not been verified by simulations yet. To remedy to these shortcomings, the present model, based on Kim et al.'s work, is structured as an interactive assembly of 3 sub-models, as shown in Fig. 1.

2.1.1. Sub-model 1: 3D cell degradation chemical reactions

This sub-model considers the physicochemical mechanisms leading to thermal runaway to predict the chemical heat released by the exothermic reactions related to the degradation of the various cell components in extreme operating conditions, using Equation (1):

$$\dot{Q}_{abuse} = \dot{Q}_{SEI} + \dot{Q}_{ne} + \dot{Q}_{pe} + \dot{Q}_{e} \quad (1)$$

where the volumetric heat generation rates of the degradation reactions are denoted $\dot{Q}_{SEI}$ for the SEI, $\dot{Q}_{ne}$ for the negative electrode, $\dot{Q}_{pe}$ for the positive electrode, and $\dot{Q}_{e}$ for the electrolyte. Each volumetric heat generation rate is calculated according to the following relation:

$$\dot{Q}_i = H_i \; W_i \; R_i \quad (2)$$

where H_i (J g^{-1}) is the specific heat release, W_i is the specific active material content (g m^{-3}) and R_i (s^{-1}) is the reaction rate in cell component *i*. The reaction rates obey the following Arrhenius laws (Equations (3)–(6)) [6,22]:

$$R_{SEI} = -\frac{dc_{SEI}}{dt} = A_{SEI} \exp\left[-\frac{E_{a,SEI}}{RT}\right] c_{SEI}^{m_{SEI}} \quad (3)$$

where c_{SEI} is the normalized concentration of metastable species containing Li in the SEI layer, A_{SEI} (s^{-1}) is the frequency factor of the SEI decomposition reaction, $E_{a,SEI}$ (J mol^{-1}) its thermal activation energy, and m_{SEI} the order of the reaction.

$$R_{ne} = \frac{dt_{SEI}}{dt} = -\frac{dc_{ne}}{dt} = A_{ne} \exp\left[-\frac{t_{SEI}}{t_{SEI,ref}}\right] c_{ne}^{m_{ne}} \exp\left[-\frac{E_{a,ne}}{RT}\right] \quad (4)$$

in which the increase in normalized thickness of the SEI, t_{SEI}, is expressed as a function of the normalized concentration, c_{ne}, of Li intercalated in the negative electrode, the frequency factor, A_{ne} (s^{-1}), of the reaction, the activation energy, $E_{a,ne}$ (J mol^{-1}), and the order, m_{ne}, of the reaction. The SEI normalized thickness is defined as $t_{SEI,0}$ ($\delta_{SEI}/\delta_{SEI,0}$), where δ_{SEI} is the SEI thickness and the subscript 0 indicates the initial value. The $t_{SEI,ref}$ parameter allows the diffusion limitation of the SEI growth to be taken into account. It is sometimes considered equal to the initial dimensionless thickness of the SEI layer [23] but other authors use it as an independent tunable parameter [6]. In the present work, this parameter was set to 1 and the other parameters of the negative electrode degradation reaction were fitted consequently.

$$R_{pe} = \frac{d\alpha}{dt} = A_{pe} \; \alpha^{m_{pe}^{p}} (1-\alpha)^{m_{pe}^{r}} \exp\left[-\frac{E_{a,pe}}{RT}\right] \quad (5)$$

where α is the degree of conversion of the active material of the positive electrode, A_{pe} (s^{-1}) and $E_{a,pe}$ (J mol^{-1}) are the reaction kinetic parameters and m_{pe} is the reaction order.

$$R_e = -\frac{dc_e}{dt} = A_e \exp\left[-\frac{E_{a,e}}{RT}\right] c_e^{m_e} \quad (6)$$

where c_e is the dimensionless concentration of electrolyte, A_e (s^{-1}) and $E_{a,e}$ (J/mol) are the kinetic parameters of the electrolyte decomposition reaction and m_e is the reaction order.

The kinetic parameters of the degradation reactions were extracted both from literature data and the experimental test carried out in this work.

2.1.2. Sub-model 2: 0D calendar ageing

Multiple and complex ageing mechanisms have been described for various chemistries of positive and negative electrodes. The mechanism considered in the present model reflects the growth of the SEI at the negative electrode since it has been identified as the main cause of calendar ageing of graphite-based LIBs [24]. In this model, in which the thickness of the SEI layer is assumed uniform inside the cell (0D model), a static ageing approach has been followed to evaluate the thickness of

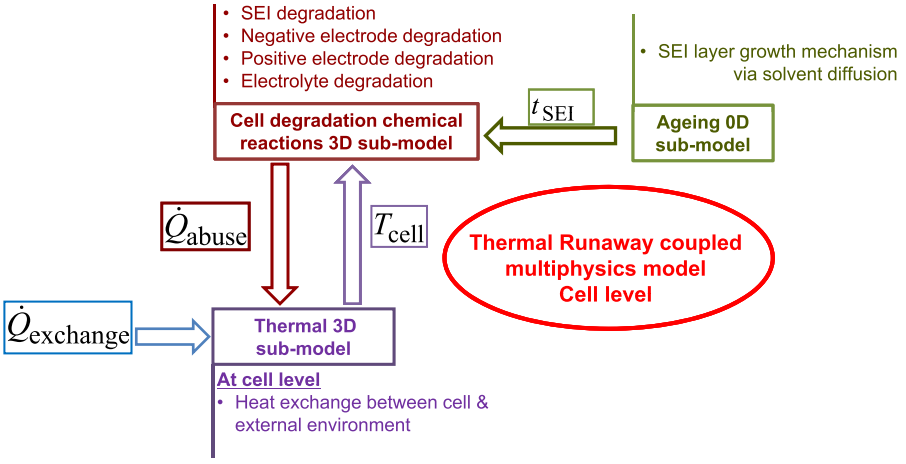

Fig. 1. Thermal runaway coupled multiphysics model.

Table 2
Models and experimental tests used in this work.

Models	Calendar ageing sub-model	Cell degradation chemical reactions sub-model	Thermal sub-model	Thermal runaway model
Experimental tests	- Initial state cell characterization - Accelerated calendar ageing - Regular check-up	Battery Test Calorimetry (for calibration)	Characterization through fine tuning thermal parameters	Oven: external heating test (for validation)

the SEI layer corresponding to a specific cell state of health. This approach does not take into account the ageing conditions of the cell and is based on the assumption that the capacity loss measured was entirely due to the SEI growth.

The SEI growth mechanism leading to calendar ageing is limited to the solvent (S) reduction at the surface of the negative electrode active material [24], according to the following reaction:

$$S + 2\,e^- + 2\,Li^+ \rightarrow P \quad (7)$$

The amount of SEI formed can be expressed using Faraday's law as a function of the cell capacity loss C in Coulomb:

$$n_{SEI} = C\frac{1}{2F} \quad (8)$$

so that the volume change of SEI can be derived from the change in capacity loss:

$$dV_{SEI} = \frac{M_{SEI}}{\rho_{SEI}} dC \frac{1}{2F} \quad (9)$$

where M_{SEI} and ρ_{SEI} are the molar mass and density of the film, respectively. To estimate the increase in SEI thickness, $d\delta_{SEI}$, it is assumed that the radius, $R_{s,n}$, of the graphite particle modeling the negative electrode is larger than the thickness of the formed SEI [24]. In that case:

$$d\delta_{SEI} = \frac{M_{SEI}}{\rho_{SEI}\, S_n} dC \frac{1}{2F} \quad (10)$$

where the electroactive surface of the negative electrode, $S_{n,}$ is given by the following equation:

$$S_n = 3\,\varepsilon_{s,n}\,\delta_n \frac{A}{R_{s,n}} \quad (11)$$

in which A is the geometric area of the negative electrode (assumed to be flat), δ_n its thickness and $\varepsilon_{s,n}$ the volumic fraction of carbon [24].

Integration of Equation (10) between times 0 (initial state) and t (calendar ageing state) gives the relationship between the thickness of the SEI layer, δ_{SEI}, and the cell capacity loss, C_{loss}, induced by calendar ageing:

$$\delta_{SEI}(t) = \delta_{SEI,0} + \frac{M_{SEI}}{\rho_{SEI}\, S_n} C_{loss} \frac{1}{2F} \quad (12)$$

2.1.3. Sub-model 3: 3D-thermal model

This sub-model is based on the energy balance equation involving the different heat sources in the core of the battery cell:

$$\rho\ C_p \frac{\partial T}{\partial t} = \dot{Q}_{abuse} + k_r \frac{\partial^2 T}{\partial r^2} + k_z \frac{\partial^2 T}{\partial z^2} \quad (13)$$

where $\dot{Q}_{abuse}$ is provided by the sub-model of cell degradation chemical reactions (Equation (1)), ρ is the density of the cell, C_p its mean thermal capacity, T its temperature, and k_r, k_z are the thermal conductivities in the radial and vertical directions of the cylindrical cell, respectively. The heat exchange between the cell and its external environment is integrated in the boundary conditions expressed by Equation (14):

$$-k_n \frac{\partial T}{\partial n} = \dot{Q}_{exchange} = h_{conv}(T_{skin} - T_{ext}) + \varepsilon\ \sigma\ (T_{skin}^4 - T_{ext}^4) \quad (14)$$

where h_{conv}, ε, σ, T_{skin}, and T_{ext} are the convective heat transfer coefficient, the emissivity of the cell surface, Stefan-Boltzmann's constant, and the skin and ambient temperatures, respectively. The left-hand side term represents the conductive heat flux from the cell core in the direction n ($n = r, z$) while the right-hand side term is the sum of the convective and radiative heat transfer rates. For simplification, this sum was written as h_{eq} (T_{skin} - T_{ext}) in this study, where h_{eq} is an equivalent heat transfer coefficient. With such assumption, the thermal exchanges were correctly described for the battery cell but this would not be the case for a battery module or pack.

In order to calibrate the thermal sub-model, the thermal properties of the cell under investigation (heat capacity C_p in J kg^{-1} K^{-1}, thermal anisotropic conductivity k in W m^{-1} K^{-1}, and heat transfer coefficient h in W m^{-2} K^{-1}) were estimated by fitting experimental data obtained from thermal characterization tests in a BTC.

The sub-models described in sections 2.1 have been ultimately coupled to achieve a multi-physics predictive model of the thermal runaway of fresh and aged Li-ion cells. This model was implemented on Comsol Multiphysics platform with fit-to-purpose experimental calibration and validation procedures for the cell under study, as described in the following section.

2.2. Experimental study

Several experimental tests were performed to calibrate and validate the thermal runaway model and sub-models, as indicated in Table 2.

2.2.1. Calendar ageing characterization

The initial state of the cells under investigation was characterized by their capacity and internal resistance before accelerated ageing. The actual capacity of each cell was determined through two charge/discharge cycles. The charge was performed successively at a constant current rate of 1 C until a 3.6 V cell voltage, and at a constant voltage of 3.6 V until the current was lower than 0.115 A (C/20). The discharge was performed at a constant current rate of 1 C until a 2 V cell voltage. The internal resistance was determined from the voltage relaxation after a discharge current step of 2 C rate during 1 s on cells charged at a 50% SOC. A 50 V - 200 A Digatron test bench and a Biologic multipotentiostat were used in addition to climatic chambers thermo-regulated at 25 °C for the experimental electrical characterization of the cells.

Accelerated calendar ageing of the cells under investigation was obtained by placing fully charged cells in a climatic chamber thermo-regulated at 60 °C. Considering an end of first life for LIBs usually consisting in 20% capacity loss, two levels of cell capacity loss, 10% and 30% corresponding respectively to mid-range of first life and to beginning of second life, were targeted and obtained by means of periodic measurements of remaining capacity all along the accelerated calendar ageing process. Higher capacity losses were not considered in this work since ageing phenomena other than the SEI growth would require the development of new sub-models. The cells collected after 75 (resp. 340) days of calendar ageing showed a capacity loss of 10% ± 3% (resp. 30% ± 3%).

2.2.2. Experimental calibration of the degradation chemical reactions sub-model

The calibration of the degradation chemical reactions parameters was performed using a BTC to ensure pseudo-adiabatic experimental conditions. The BTC (HEL Company, Hertfordshire, UK) had a cylindrical test chamber (diameter 35 cm and height 32.5 cm) heated on all sides (bottom, top and lateral). The tested cell was positioned in the center of the BTC enclosure. Two type-K thermocouples were placed on the negative and positive electrode sides of the cell to monitor the cell surface temperature during the test. The cell was then covered with an aluminum foil to ensure good heat diffusion and finally surrounded by a heater wire of length 1 m and resistance 11 Ω. The energy for heating the cell was provided by the heater wire while the energy for heating the climatic chamber was provided by the BTC, both heating procedures being controlled by the program operating the BTC. The cell voltage was also monitored during the test.

To determine the onset of self-heating, the BTC was operated with a MultiRamp program similar to the well-known HWS (heat, wait, search) mode. In this study, fully charged cells were first heated up to a temperature of 30 °C before a calibration step of 90 min. Then, the temperature was increased in discrete steps of 5 °C, each of them (under safe behavior of the cell) followed by a 30 min long wait step during which the cell was held at constant temperature to reach complete thermal equilibrium with the calorimetric system. If the cell temperature did not increase at a rate above a threshold value, typically 0.02 °C/min, indicating no adverse thermal event, the temperature was increased by another heating step and the algorithm was repeated as needed until some exothermal reaction occurred. By contrast, if the cell temperature increased at a rate above the mentioned threshold value during the wait step, the BTC switched to the exothermic mode during which its temperature closely matched the cell temperature, thus maintaining the adiabatic state. This was followed by search step of 10 min during which the system tried to detect any self-heating phenomena on the cell surface. The experiments in the BTC were terminated by cooling the cell once it reached its upper temperature limit of 350 °C. Thanks to the adiabatic conditions and the stepwise process allowing the observation of individual self-heating reactions, this procedure allowed the reaction rate parameters of the different exothermic reactions degrading the cell components during a thermal runaway to be determined.

The use of oven tests is very frequently reported in the literature, particularly to apply thermal abuse conditions on the investigated cells in a well-controlled environment, which allows experimental validation of thermal runaway models [6,21,22,25–27]. In such tests, cells are heated to excessive temperatures in order to examine their thermal stability performance. Being closer to actual environmental conditions (no adiabaticity), oven tests were used in this work to validate the thermal runaway model. The tested cell was placed in the center of a thermostatically controlled oven (*France Etuves*, model XL 1000) and the air was circulated at full speed to obtain a uniform temperature around the cell. Up to five type-K thermocouples were fixed on the cell surface (two on the positive and negative electrodes and three on its lateral surface) and four additional thermocouples were installed to measure the oven temperature. The oven was first preheated to the target cell temperature of 30 °C that was maintained during 60 min. Thereafter, the cell temperature was increased at a rate of 5 °C/min until the activation of thermal runaway or the observation of a plateau value of 200 °C stabilized during 2 h as a proof of a complete reaction of the cell. The surface temperature of the cell was measured at a sample rate of 1 Hz with a data logger.

2.2.3. Influence of ageing on the cell degradation chemical reactions

As an example, Fig. 2 shows the evolution of the surface temperature of a fresh A123 cell and its voltage during the test in the BTC. Three critical temperatures can be identified [15]:

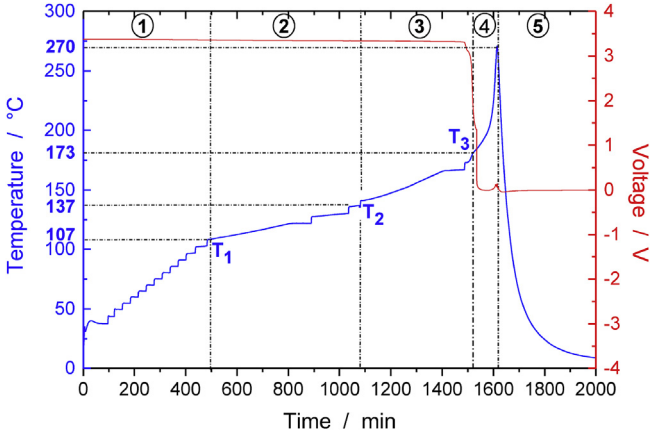

Fig. 2. Surface temperature and voltage of a fresh A123 battery cell measured during the calibration experiment in the BTC.

- the initial self-heating temperature, T_1, related to the SEI layer decomposition reaction: it is important to note that its detection depends on the accuracy and sensitivity of the testing device and also on the threshold detection value indicated in the BTC operating program (0.02 °C/min for exothermic reaction in this work).
- the starting temperature, T_2, of the melting process of the battery separator material: this temperature was detected by the endothermic reaction indicated by the hardly visible decrease of the recorded temperature at time 1077 min. It is known that the melting point of commercial separator materials is expected to range between 130 °C and 160 °C depending on their composition. Above this critical temperature the separator loses its mechanical integrity and starts to induce internal micro short-circuits.
- the thermal runaway trigger temperature, T_3: the accelerated increase in temperature was caused by the heat released by the exothermic reactions and by the occurrence of short circuits, as shown by the steep decrease of the cell voltage.

Fig. 2 shows five stages in the evolution of the cell temperature: (1) end of safe state, (2) and (3) still reversible self-heating regions, (4) triggering of thermal runaway, and (5) cell cooling down. However, the peaks detected do not allow a clear identification of the corresponding degradation reactions of the cell components.

Several such experiments were performed in the BTC with fresh and aged A123 cells to investigate the influence of ageing on thermal runaway. Table 3 represents the three critical temperatures averaged for 3 fresh cells, 1 cell aged at 10% and 3 cells aged at 30%. The data were collected using the procedure described in Section 2.2.2. The results show that T_1 increased with ageing, indicating that a higher temperature is needed to cause the onset of self-heating. In contrast, T_3 decreased with increasing ageing, which means that the aged cells underwent thermal runaway at a lower temperature than fresh cells. As for T_1, the critical temperature T_2 related to the separator melting process increased with ageing, which might be caused by mechanical stress generated during the ageing process. However, the effect of ageing on the cell separator is currently not well known and would deserve more investigation. It is not possible to conclude on the positive

Table 3
Evolution of the critical temperatures related to the thermal safety of A123 cells with ageing (from experimental data in the BTC).

Temperature	T_1 (°C)	T_2 (°C)	T_3 (°C)
Fresh	79.7	137.7	171.3
Aged at 10%	83	145.7	154
Aged at 30%	92	147	150.7

effect of ageing on the thermal safety of the cells in spite of the delayed self-heating process. All the parameters examined here are important and have to be considered to improve the safety management of battery cells during their entire lifetime in various operating conditions [13].

3. Model calibration and validation

3.1. Model implementation and parameters setting

The thermal runaway model was developed for a cylindrical 26650 LFP/C cell. Since the battery cell case is made of metal with very good thermal conductivity and very small thickness (< 1 mm), its thermal influence was neglected and subsequently only the electrochemical part of the cell (positive electrode, negative electrode, and electrolyte) was considered in the modeling work. Moreover, the battery internal spiral wound structure was not introduced in the model so that the cell was considered as a homogenous system with equivalent thermal parameters for the different materials, as in the approach used by Chen et al. [28]. This approximation made it possible to reduce the number of input parameters needed to operate the model and to simplify its geometry. However, the anisotropy of the thermal conductivity was actually taken into account. Typically, the thermal conductivity can be several tens of times less in the radial direction than in the axial direction. The equivalent thermal parameters given in Table 4 were determined by fitting experimental data obtained on a battery cell in quasi-adiabatic conditions in an accelerated rate calorimeter with a simple thermal model based on Equation (13).

The geometry of the cylindrical battery cell being simple, a regular mesh was used with 1129 domain elements, 424 boundary elements, and 80 edge elements. The 3D thermal sub-model giving the evolution of the temperature gradient in the entire cell was implemented using the Heat Transfer in Solids module, in which the energy balance in the core of the cell (Equation (13)) corresponds to the differential form of the Fourier equation. Equations (3)–(6) accounting for the chemical degradation processes characterizing the thermal runaway were solved using the ODE (Ordinary Differential Equations) module to evaluate the temporal evolution of the concentrations of the species involved in the exothermic reactions. The equations were solved locally at each node of the mesh. Both chemical and thermal sub-models were coupled since the abuse heat source term given by the chemical sub-model was an input of the thermal sub-model.

3.2. Model calibration

The model was first calibrated for fresh A123 battery cells from experiments performed in the BTC to determine the degradation chemical reaction parameters (Table 5). For that, a lumped model, in which variables are considered uniform and only depend on time, was used to save calculation time without losing efficiency, as shown in a comparative study by Kim et al. [6]. This model allows the temperature of a LFP/C cell to be simulated in pseudo-adiabatic conditions representative of thermal abuse tests in a BTC in which the model input is the heat power provided by the heater wire surrounding the cell and the model output is the cell surface temperature defined as the average temperature of the two thermocouples.

Table 5
Parameters of the degradation chemical reaction model for the A123 LFP/C cells: (a) fitted from our calibration work, (b) from Ref. [6], (c) from Ref. [29], (d) calculated.

Parameters		LFP/C (A123)	LFP/C (Literature)
Activation energy values (J mol^{-1})	$E_{a,SEI}$	1.38×10^5 (a)	1.35×10^5 (b)
	$E_{a,ne}$	1.32×10^5 (a)	1.35×10^5 (b)
	$E_{a,pe}$	0.99×10^5 (a)	1.03×10^5 (c)
	$E_{a,e}$	2.70×10^5 (a)	2.74×10^5 (b)
Reaction factors (s^{-1})	A_{SEI}	1.66×10^{15} (b)	1.66×10^{15} (b)
	A_{ne}	2.50×10^{13} (b)	2.50×10^{13} (b)
	A_{pe}	2×10^8 (c)	2×10^8 (c)
	A_e	5.14×10^{25} (b)	5.14×10^{25} (b)
Reaction orders (−)	m_{SEI}	1(b)	1(b)
	m_{ne}	1(b)	1(b)
	m_{pe}^p, m_{pe}^r	1(b)	1(b)
	m_e	1(b)	1(b)
Initial values of key variables (−)	$c_{SEI,0}$	0.15(b)	0.15(b)
	$c_{ne,0}$	0.75(b)	0.75(b)
	α_0	0.04(b)	0.04(b)
	$c_{e,0}$	1(b)	1(b)
	$t_{SEI,0}$	0.033(b)	0.033(b)
Heat released (J kg^{-1})	H_{SEI}	$2.57 \times 10^{5(b)}$	$2.57 \times 10^{5(b)}$
	H_{ne}	$1.714 \times 10^{5(b)}$	$1.714 \times 10^{6(b)}$
	H_{pe}	$1.947 \times 10^{5(c)}$	1.947×10^5 (c)
	H_e	6.2×10^5 (a)	1.55×10^5 (b)
Specific active material content (kg m^{-3})	$W_{n,e}$	220(d)	1700(b)
	$W_{p,e}$	520.74(d)	960(c)
	W_e	334.68(d)	500(b)

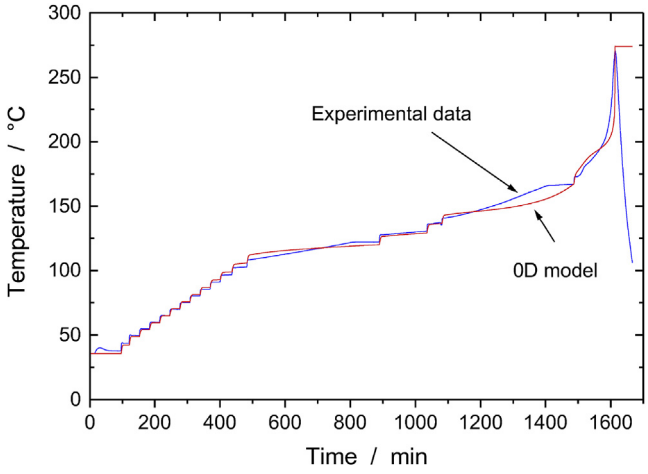

Fig. 3. Comparison of the simulated average surface temperature of a fresh A123 battery cell with the experimental data in Fig. 2.

Fig. 3 presents the simulated evolution of the surface temperature of the fresh cell shown in Fig. 2. The kinetic parameters (Table 5) have mostly been taken from literature [6,29]. However, the specific carbon content in the negative electrode, $W_{n,e}$, and the specific active material content in the positive electrode, $W_{p,e}$, were calculated from ante

Table 4
Thermal parameters of the A123 cells.

Capacity Ah	Density ρ (kg/m^3)	Heat capacity C_p (J kg^{-1} K^{-1})	Heat transfer h_{eq} (W K^{-1} m^{-2})	Thermal conductivity	
				Radial k_r (W K^{-1} m^{-1})	Axial k_z (W K^{-1} m^{-1})
2.3 Ah	2231.2	1100	20	0.7	140

Table 6
Parameters of the calendar ageing model for the A123 LFP/C cells: (a) from Ref. [24], (b) from Ref. [6], (c) calculated.

Parameters		A123
M_{SEI} (kg mol^{-1})		0.162[(a)]
ρ_{SEI} (kg m^{-3})		1690[(a)]
$\varepsilon_{s,n}$		0.58[(a)]
δ_n (m)		3.45×10^{-5} [(a)]
A (m^2)		0.18[(a)]
$R_{s,n}$ (m)		5×10^{-6} [(a)]
C_{loss} (Ah)	10% capacity loss	0.23[(c)]
	30% capacity loss	0.69[(c)]
F (C mol^{-1})		96485
$\delta_{SEI,0}$ (m)		5×10^{-9} [(a)]
$t_{SEI,0}$ (dimensionless)		0.033[(b)]
$\delta_{SEI\ (10\%\ capacity\ loss)}$ (m)		1.98×10^{-7} [(c)]
$t_{SEI\ (10\%\ capacity\ loss)}$ (dimensionless)		1.31[(c)]
$\delta_{SEI\ (30\%\ capacity\ loss)}$ (m)		5.84×10^{-7} [(c)]
$t_{SEI\ (30\%\ capacity\ loss)}$ (dimensionless)		3.86[(c)]

mortem analysis of A123 cells performed in the Simcal project [30] while the specific active material content in the electrolyte, W_e, was chosen as 20% of that of the whole cell. Large differences can be noted between the values of $W_{n,e}$ and $W_{p,e}$ compared to literature values, while the W_e values are closer. Moreover, the specific heat released from the electrolyte, H_e, was fitted from the experimental data since the solvent composition of the electrolyte in the A123 cells identified in the Simcal project was different from that of the electrolyte in the literature [29]. The values of the activation energies,$E_{a,SEI}$, $E_{a,ne}$, $E_{a,pe}$, $E_{a,e}$, were also fitted from the experimental data. Indeed, the exothermic degradation reactions of the different cell components (SEI, negative electrode, positive electrode and electrolyte) occur in cascade. It is then difficult to identify them separately using the BTC data, all the more so as the first two reactions related to the SEI and to the negative electrode are correlated through the $W_{n,e}$ parameter. In addition, the degradations of the positive electrode and electrolyte solvent are coupled.

For the calendar ageing model, no parameter was fitted from experimental data. As shown in Table 6, most of the parameters were taken from literature. The dimensionless thickness, t_{SEI}, of the SEI layer formed at the two levels of accelerated calendar ageing considered in this work (10% and 30% capacity loss) are also reported. These parameters, which were calculated from Equations (11) and (12), are the inputs of the cell degradation chemical reactions sub-model. In other words, the only effect of calendar ageing on thermal runaway was the change in value of the initial thickness of the SEI layer used in Equation (4), as described in Table 6.

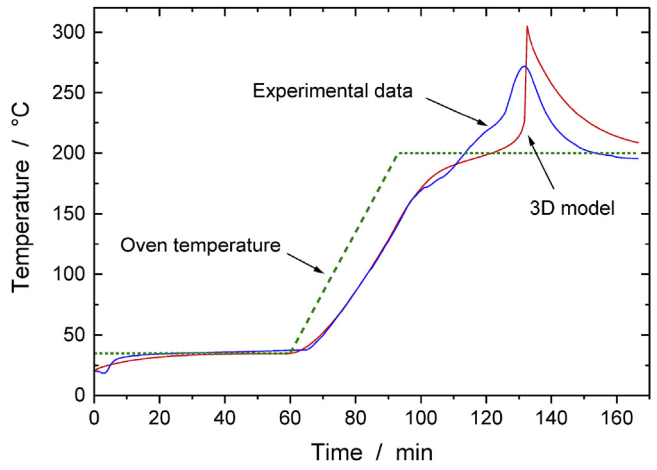

Fig. 4. Experimental and simulated evolution of the average surface temperature of a fresh A123 cell during the oven test.

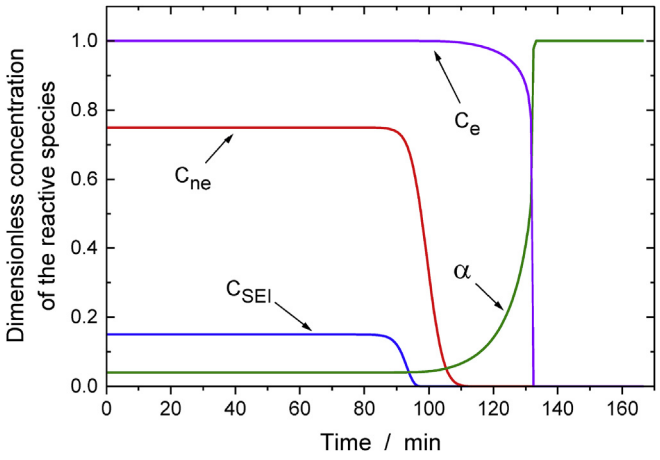

Fig. 5. Simulated evolution of the dimensionless concentrations of the reactive species during the oven test.

3.3. Model validation

The calibrated thermal runaway model for the LFP/C chemistry was then validated for A123 cells with overheating tests carried out in the oven. Fig. 4 compares the experimental cell surface temperature measured during the oven test to the average surface temperature simulated with the thermal runaway 3D model. At first glance, it comes out that both temperature curves have a similar form even if the model better fits measured temperatures evolution at the beginning of the simulation (up to $t \approx 100$ min), than during the later stages of the thermal runaway process. Fig. 5 shows the corresponding evolution of the dimensionless average volume concentration and degree of conversion of the chemical species. It can be noted from the c_{SEI} and c_{ne} variations that the chemical degradation of the SEI and negative electrode occurred at times between $t = 90$ and 100 min. Indeed, until that time the cell temperature prediction was in good agreement with the experimental data according to Fig. 4. By contrast, the major degradation of the electrolyte reflected in Fig. 5 by the steep c_e decrease occurred beyond $t = 100$ min where the predicted cell temperature significantly differs from the temperature measured in the oven test. The current limitation in the prediction capability of the model is mainly related to the poor estimation of the kinetic parameters associated to the complex degradation process of the electrolyte. However, a slight loss of airtight integrity of the oven door due to its deformation under thermal stresses was observed at a temperature around 170 °C. This could be, at least partly, at the origin of the limited thermal dissipation that caused a slower increase in the measured temperature of the cell surface at $t = 100$ min (see Fig. 4). This thermal loss is obviously not taken into account in the model and results in the overestimation of the simulated peak temperature of the cell under the operating conditions.

Some other limitations and shortcomings related to the validation process of the model should be mentioned in addition to the fact that the model considers only the contribution of the degradation chemical reactions of the cell components during thermal runaway. Under abuse testing conditions, the cylindrical cells were observed to vent once a critical internal pressure was reached. In such conditions, the further heating of the cell results in vaporization of the organic solvents used in the electrolyte. Additional degradation chemical reactions between the electrolyte and the cell components also lead to accelerated gas generation. Depending on the overpressure reached, cell venting can lead to ejection of the electrolyte or even the jellyroll contents. Thus, the heat dissipation and the reactive mass loss due to such ejection should be considered in a more robust thermal runaway model as shown by Coman et al. [23] in their lumped model of venting during thermal runaway for a cylindrical LCO cell. During the experimental study, separator melting was observed to lead most of the time to almost

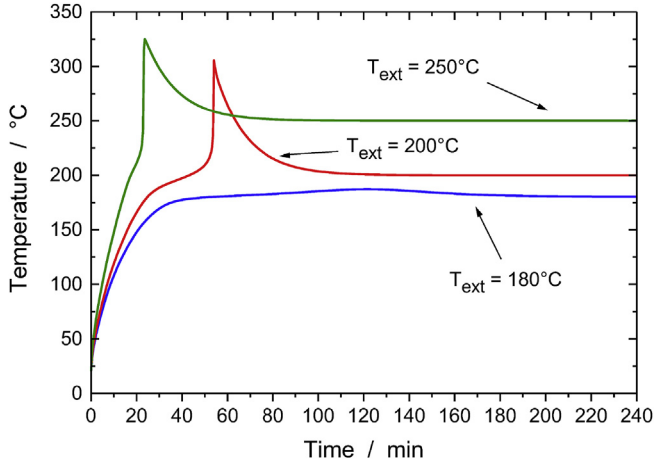

Fig. 6. Simulation of the average surface temperature of a fresh A123 cell as a function of the external temperature (h_{eq} = 20 W K^{-1} m^{-2}).

immediate strong internal short circuit, which is not taken into account in the present model, and then to the associated thermal runaway. Contribution of internal short circuits could be considered in an improved version of the model by introducing a specific electrochemical sub-model or localized hot spots in the thermal model with corresponding heat releases.

4. Simulation results and discussion

Using this calibrated and validated modeling approach for the A123 cells, it is then possible with computer simulations to better understand the thermal runaway mechanism and to investigate the influence of battery ageing on this destructive phenomenon.

4.1. Thermal runaway onset temperature

Fig. 6 shows computer simulations of the average surface temperature of a fresh cell for different values of the external temperature, which is the parameter of major influence on thermal runaway. The initial temperature value was fixed at 20 °C, and various abuse external temperatures (from 180 °C to 250 °C) were set as single increments at t = 0 min. The heat exchange coefficient, h_{eq}, was set at 20 W K^{-1} m^{-2} as in the oven test (Fig. 4), which corresponds to forced convection conditions. At the beginning of the simulation, the cell average surface temperature increased at the same rate, independently of the external temperature. Then, for T_{ext} = 250 °C the cell temperature rapidly reached a peak temperature of 335 °C, indicating that thermal runaway occurred under these conditions, before decreasing, to stabilize at the external temperature of 250 °C. For T_{ext} = 200 °C the simulation shows a decrease in the cell heating rate between 180 °C and 200 °C, and a rapid increase from t = 40 min to reach 300 °C in 10 min before cooling down. In contrast, for T_{ext} = 180 °C, the cell temperature increased gradually from t = 30 min up to 185 °C and did not undergo thermal runaway.

It can be concluded that the higher the external temperature, the higher the probability to initiate a thermal runaway, and the higher the severity of this thermal event. It has also been found that there is a critical temperature below which the cell does not go on thermal runaway.

4.2. Effect of heat transfer on thermal runaway

According to Fig. 6, below a critical external temperature, $T_{ext,c}$, ranging between 180 °C and 200 °C, no thermal runaway occurs. However, the result was shown for an equivalent heat transfer of rather high

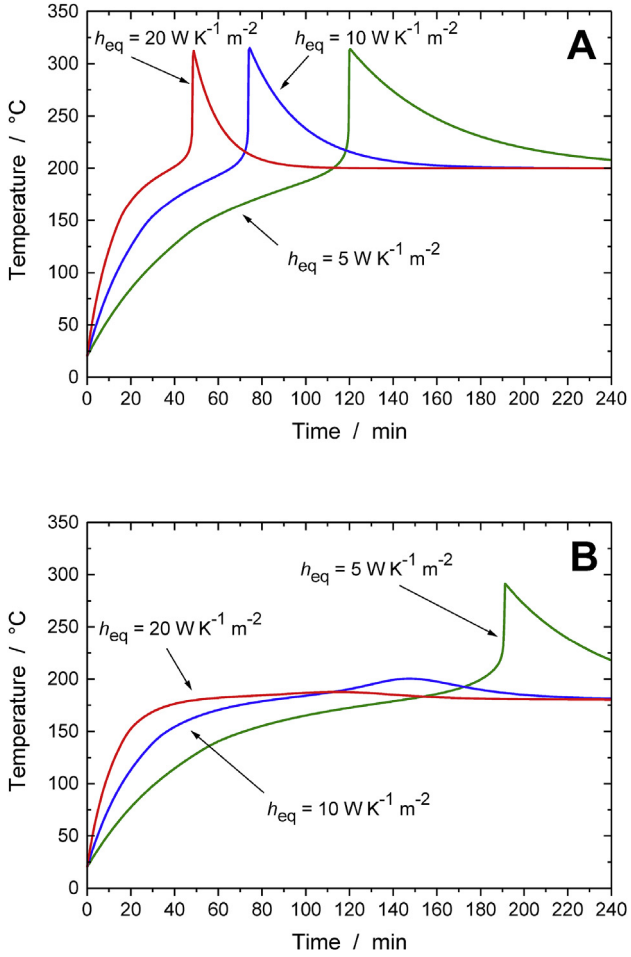

Fig. 7. Influence of the equivalent heat transfer coefficient on the average surface temperature of a fresh A123 cell: T_{ext} = 200 °C (A), T_{ext} = 180 °C (B).

value (h_{eq} = 20 W K^{-1} m^{-2}). It is then important to investigate the influence of this coefficient on the surface temperature of the cell as a function of the external temperature [21]. Fig. 7 shows the evolution of the average surface temperature of a fresh cell for two values of the external temperature, 180 °C and 200 °C, and several values of h_{eq}. When the external temperature is higher than $T_{ext,c}$ (Fig. 7A), thermal runaway takes place for all values of the heat transfer coefficient since the cell reaches temperatures around 200 °C at which violent degradation reactions already occurred, as that of the electrolyte. So, the external temperature is excessive for the cell even when decreasing the heat exchange, which only delays the time to reach 200 °C and, therefore, thermal runaway. In contrast, when the external temperature is lower (180 °C), no thermal runaway is expected according to Fig. 6 but the simulations in Fig. 7B show it does occur when the heat exchange is too low, due for example to a failure of the cooling system, to dissipate the heat outside the cell and prevent it from reaching abuse temperatures.

4.3. Effect of ageing on thermal runaway

The effect of accelerated calendar ageing on thermal runaway is analyzed through simulations of the cell temperature of cells aged at 10% and 30% of capacity loss exposed at an oven temperature T_{ext} = 180 °C and a low heat exchange (h_{eq} = 5 W K^{-1} m^{-2}). As for the fresh cell in Fig. 7B, the initial temperature of the cell is 20 °C and the only difference is the thickness of the SEI layer corresponding to the ageing state (see Section 3.2 and Table 6). Fig. 8A shows a slower temperature increase for the aged cells from 60 to 140 min when the cell is mainly heated by the simulated oven up to a temperature of

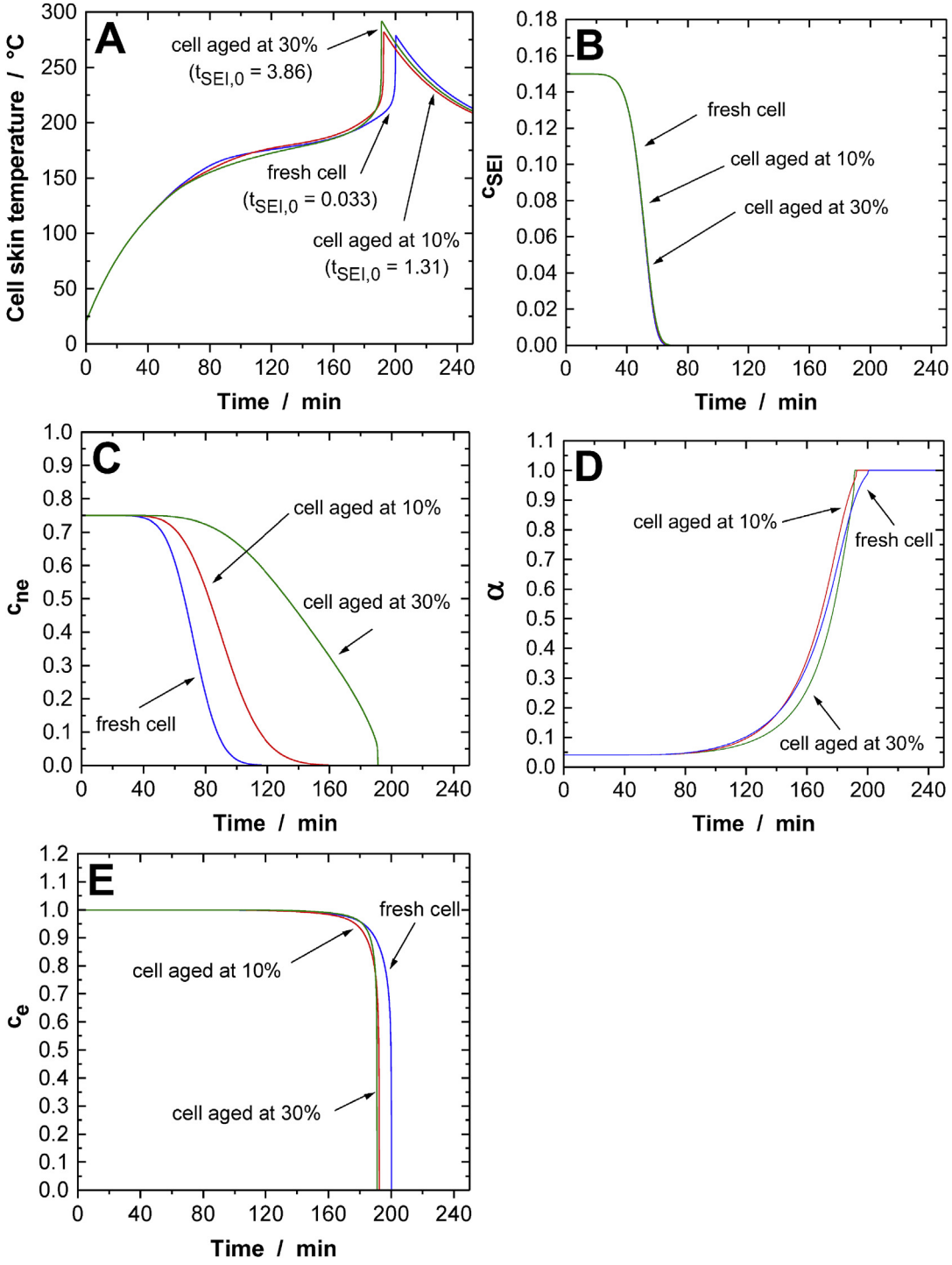

Fig. 8. Simulated evolution of the cell average surface temperature (A) and dimensionless concentrations of the reactive species (B to E) during the oven test (T_{ext} = 180 °C, h_{eq} = 5 W K^{-1} m^{-2}).

180 °C. From that time, the cell is heated by the degradation reactions and its temperature increases faster for the aged cells, before decreasing down to the temperature of the oven once the degradation reactions are complete. These results are consistent with those observed experimentally (Table 3).

To get a deeper understanding of the evolution of the cell temperature, Fig. 8B–E shows the effect of ageing on the average volume concentrations of the reactive species. It can be seen in Fig. 8B and C that the degradation reactions of the SEI and the negative electrode take place between 60 and 140 min for the fresh cell, causing a slight temperature increase at about 80 min. As a consequence, after 140 min only two exothermal reactions happen (degradation of the positive electrode and electrolyte, see Fig. 8D and E) instead of three for the aged cells since reactants are still present in the negative electrode at time 140 min (2.4% and 43.6% for the cells aged at 10% and 30%, respectively). Moreover, the power released by the aged cells is more important and their temperature increases faster and higher than for the fresh cell. The delay in degradation of the negative electrode can be explained by increased diffusional limitations of Li ions due to a thicker SEI layer after accelerated calendar ageing.

5. Conclusion

No model able to predict thermal runaway regardless its origin (electrical, thermal or mechanical abuse) has yet been published. No model either takes into account all physical phenomena involved in a Li-ion battery or considers all heat generation sources inside the battery. Moreover, most of past studies deal with fresh materials or new cells only. Nevertheless, for using Li-ion batteries in growing high energy demanding applications, it is a key issue to guarantee safety for the entire lifetime of batteries and also for their second life targeting less demanding applications. The present work is a step forward in understanding the thermal behavior of an aged LIB cell.

To investigate the mechanisms leading to thermal runaway, especially for aged Li-ion batteries, it was necessary to adopt a strategy combining modeling and experimental work to achieve a multiphysics 3D model of thermal runaway of fresh and aged LIB cells. The model was structured into three coupled sub-models, a 3D thermal model, a 3D degradation chemical reaction model, and a 0D calendar ageing model based on a simplified SEI growth mechanism. This model was developed at the cell level and calibrated for the LFP/C chemistry. The thermal parameters were fitted from experimental data while the kinetics model parameters were taken from literature or fitted from calorimetric tests. Accelerated calendar ageing tests allowed the calibration of the ageing model at two different levels of capacity loss. The loss thermal runaway model including ageing was then validated for commercialized A123cylindrical cells by comparing simulations to cell responses measured in oven abuse tests.

The primary effect of accelerated calendar ageing on the thermal stability of A123 cells was shown to be the onset of the first exothermic reaction at a higher temperature for the aged cells. In addition, the aged cells were revealed to undergo thermal runaway at a lower temperature than new cells. Computer simulations were able to reproduce these experimental results. Moreover, the simulated evolution of the reactive species concentration provided evidence of the relationship between the diffusional limitations generated by the growth of the SEI layer induced by calendar ageing and the delay of the self-heating onset temperature. Besides calendar ageing considered in this work, it is important to investigate the influence of other ageing processes on thermal stability, as for example Li-plating that is expected to be faced in high energy cells.

Other perspectives can be put forward to improve the thermal runaway model. Some events observed during the abuse tests, which would deserve due consideration, are not yet included in the current version of the model, such as the separator melting process and cell venting. Separator melting, which causes an internal short circuit that triggers the cell thermal runaway can be treated by considering the internal short circuit as a localized hot spot in a future refinement of the thermal runaway model. The development of a coupled electrochemical-thermal short circuit model would also deserve a dedicated research effort. With regard to the cell venting issue, it could be taken into account by introducing a pressure dependent relationship associated with the evaporation of the electrolyte solvent. Calibration of the model for application to other chemistries is obviously another direction for future work towards a more valuable tool to optimize the design of lithium-ion batteries for safety management purposes.

References

[1] K. Smith, G.-H. Kim, E. Darcy, A. Pesaran, Int. J. Energy Res. 34 (2010) 204–215.
[2] D. Doughty, E.P. Roth, Interface, Electrochem. Soc. (Summer 2012) 37–44.
[3] Y.-S. Duh, K.H. Lin, C.-S. Kao, J. Therm. Anal. Calorim. (2018), https://doi.org/10.1007/s10973-018-7077-2.
[4] M.J. Loveridge, G. Remy, N. Kourra, R. Genieser, A. Barai, M.J. Lain, Y. Guo, M. Amor-Segan, M.A. Williams, T. Amietszajew, M. Ellis, R. Bhagat, D. Greenwood, Batteries 4 (2018) 3 https://doi.org/10.3390/batteries4010003.
[5] D. Lisbona, T. Snee, Process Saf. Environ. Protect. 89 (2011) 434–442.
[6] G.-H. Kim, A. Pesaran, R. Spotnitz, J. Power Sources 170 (2007) 476–489.
[7] Y. Guo, Safety: thermal runaway, in: J. Garche (Ed.), Encyclopedia of Electrochemical Power Sources, vol. 4, Elsevier, Amsterdam, 2009, pp. 241–253.
[8] W. van Schalkwijk, B. Scrosati, Advances in Lithium-ion Batteries, Springer, 2002.
[9] G. Binotto, S. Genies, M. Morcrette, Review Thermal Runaway Reactions Mechanisms, HELIOS (High Energy Lithium-ion Storage Solutions) Project, FP7 2333765, European Commission, 2011, pp. 1–41.
[10] S. Al Hallaj, H. Maleki, J.S. Hong, J.R. Selman, J. Power Sources 83 (1999) 1–8.
[11] F. Del Corso, H. Mettlach, M. Morcrette, U. Koehler, C. Gousset, C. Sarrazin, G. Binotto, D. Porcellato, M. Vest, High energy lithium ion storage solutions: comparative assessment of 4 chemistries of cathode for EV and PHEV applications, in: E. Briec, B. Müller (Eds.), Electric Vehicle Batteries: Moving from Research towards Innovation, Springer, Cham, 2015, pp. 1–17 https://doi.org/10.1007/978-3-319-12706-4.
[12] M. Fleischhammer, T. Waldmann, G. Bisle, B.-I. Hogg, M. Wohlfahrt-Mehrens, J. Power Sources 274 (2015) 432–439.
[13] P. Röder, B. Stiaszny, J.C. Ziegler, N. Baba, P. Lagaly, H.-D. Wiemhöfer, J. Power Sources 268 (2014) 315–325.
[14] E.P. Roth, D.H. Doughty, J. Power Sources 128 (2004) 308–318.
[15] J. Zhang, L. Su, Z. Li, Y. Sun, N. Wu, Batteries 2 (2016) 12 https://doi.org/10.3390/batteries2020012.
[16] S. Santhanagopalan, Q. Guo, P. Ramadass, R.E. White, J. Power Sources 156 (2006) 620–628.
[17] X. Feng, M. Ouyang, X. Liu, L. Lu, Y. Xia, X. He, Energy Storage Mater. 10 (2018) 246–267.
[18] S. Abada, G. Marlair, A. Lecocq, M. Petit, V. Sauvant-Moynot, F. Huet, J. Power Sources 306 (2016) 178–192.
[19] J. Zhu, T. Wierzbicki, W. Li, J. Power Sources 378 (2018) 153–168.
[20] T.D. Hatchard, D.D. MacNeil, D.A. Stevens, L. Christensen, J.R. Dahn, Electrochem. Solid State Lett. 3 (2000) 305–308.
[21] T.D. Hatchard, D.D. MacNeil, A. Basu, J.R. Dahn, J. Electrochem. Soc. 148 (2001) A755–A761.
[22] C.F. Lopez, J.A. Jeevarajan, P.P. Mukherjee, J. Electrochem. Soc. 162 (2015) A2163–A2173.
[23] P.T. Coman, S. Rayman, R.E. White, J. Power Sources 307 (2016) 56–62.
[24] E. Prada, D. Di Domenico, Y. Creff, J. Bernard, V. Sauvant-Moynot, F. Huet, J. Electrochem. Soc. 160 (2013) A616–A628.
[25] R.M. Spotnitz, J. Weaver, G. Yeduvaka, D.H. Doughty, E.P. Roth, J. Power Sources 163 (2007) 1080–1086.
[26] G. Guo, B. Long, B. Cheng, S. Zhou, P. Xu, B. Cao, J. Power Sources 195 (2010) 2393–2398.
[27] M. Guo, R.E. White, J. Power Sources 221 (2013) 334–344.
[28] Y. Chen, J.W. Evans, J. Electrochem. Soc. 140 (1993) 1833–1838.
[29] P. Peng, F. Jiang, Int. J. Heat Mass Tran. 103 (2016) 1008–1016.
[30] A. Delaille, S. Grolleau, F. Duclaud, J. Bernard, R. Revel, S. Pélissier, E. Redondo-Iglesias, J.-M. Vinassa, A. Eddahech, C. Forgez, M. Kassem, S. Joly, D. Porcellato, P. Gyan, S. Bourlot, M. Ouattara-Brigaudet, SIMCAL Project: calendar aging results obtained on a panel of 6 commercial Li-ion cells, 224th Electrochemical Society Meeting, San Francisco, USA, 2013 Abstract 1191.